**Retina**

# Human Chorioretinal Layer Thicknesses Measured in Macula-wide, High-Resolution Histologic Sections

*Christine A. Curcio,[1] Jeffrey D. Messinger,[1] Kenneth R. Sloan,[2] Arnab Mitra,[1] Gerald McGwin,[3] and Richard F. Spaide[4]*

**PURPOSE.** To provide a comprehensive description of chorioretinal layer thicknesses in the normal human macula, including two-layer pairs that can produce a combined signal in some optical coherence tomography (OCT) devices (ganglion cell [GCL] and inner plexiform [IPL] layers and outer plexiform [OPL] and outer nuclear [ONL] layers).

**METHODS.** In 0.8-$\mu$m-thick, macula-wide sections through the foveola of 18 donors (age range, 40–92 years), 21 layers were measured at 25 locations by a trained observer and validated by a second observer. Tissue volume changes were assessed by comparing total retinal thickness in ex vivo OCT and in sections.

**RESULTS.** Median tissue shrinkage was 14.5% overall and 29% in the fovea. Histologic laminar boundaries resembled those in SD-OCT scans, but the shapes of the foveolar OPL and ONL differed. Histologic GCL, IPL, and OPLHenle were thickest at 0.8. to 1, 1.5, and 0.4 mm eccentricity, respectively. ONL was thickest in an inward bulge at the foveal center. At 1 mm eccentricity, GCL, INL, and OPLHenle represented 17.3% to 21.1%, 18.0% to 18.5%, and 14.2% to 16.6% of total retinal thickness, respectively. In donors ≥70 years of age, the RPE and choroid were 17.1% and 29.6% thinner and OPLHenle was 20.8% thicker than in donors <70 years.

**CONCLUSIONS.** In this study, the first graphic representation and thickness database of chorioretinal layers in normal macula were generated. Newer OCT systems can separate GCL from IPL and OPLHenle from ONL, with good agreement for the proportion of retinal thickness occupied by OPLHenle in OCT and histology. The thickening of OPLHenle in older eyes may reflect Müller cell hypertrophy associated with rod loss. (*Invest Ophthalmol Vis Sci.* 2011;52:3943–3954) DOI:10.1167/iovs.10-6377

The macula, a 6-mm-diameter area centered on the fovea,[1,2] comprises numerous clinically relevant layers, sublayers, and potential spaces. As classically described[1,3,4] (Fig. 1), these include (from inner to outer) the nerve fiber layer (NFL), ganglion cell layer (GCL), inner plexiform layer (IPL), inner nuclear layer (INL), outer plexiform layer (OPL), outer nuclear layer (ONL) including inner fibers, photoreceptor inner and outer segments (IS, OS; Polyak's bacillary layer[1]), and retinal pigment epithelium (RPE). The macular OPL has sublayers of bipolar cell terminals, cone pedicles, and Henle fibers (photoreceptor axons and Müller cells). Photoreceptor IS have myoid and ellipsoid compartments. Choroidal layers include the inner and outer Bruch's membrane (BrM), the choriocapillaris, and the choroid, delimited from the sclera by the lamina suprachoroidea. Stereotypic extracellular debris accumulates with aging and age-related macular degeneration (AMD) in the subretinal space (subretinal drusenoid debris), internal to the RPE basal lamina (basal laminar deposit; BlamD), and external to the RPE basal lamina (BlamD/drusen).[7–9]

The clinical diagnosis and management of macular disease, including diabetic retinopathy, veno-occlusive disease, and in the future, AMD,[10–15] has been revolutionized by optical coherence tomography (OCT).[16–18] In spectral-domain OCT (SD-OCT), light from a reference arm interferes with light backscattered from different layers. Fourier analysis of this interferogram provides tissue depth information at a resolution of 5 to 6 $\mu$m. In addition to detailed retinal cross sections, newer enhancements now display choroid.[19,20] Image validation (i.e., linking OCT signals to cell and tissue features), is important for increasing the accuracy and utility of this modality. Histology is considered the gold standard for informing and validating OCT,[21–25] even if laboratory analysis of clinically imaged eyes is not always possible.

OCT reveals alternating bands of hyper- and hyporeflectivity, not necessarily coincident with retinal layers seen by other methods (Fig. 2). Previous technologies revealed one moderately reflective band in the inner retina that did not reliably demarcate the GCL and IPL.[16,26–28] Separation of a less reflective GCL from a more reflective IPL is now more readily achieved through SD-OCT and its modifications.[29,30] The ONL, a thick hyporeflective outer retinal layer, includes inconsistently seen Henle fibers on its inner aspect.[16,26,31–34] The nomenclature linking three hyperreflective outer retinal bands to photoreceptor IS and OS, RPE, and choriocapillaris is especially controversial.[35–37] Layer assignments are not merely semantic issues, as a rich knowledge base of neurobiology, vascular biology, and pathology could be brought to bear on diagnosis and clinical management by invocation of the correct names. Variable layer names reflect challenges to validating OCT images. A major factor is the progressive disclosure of anatomic features by each new generation of instruments. Histologic validation of OCT using animal models lacking maculas,[38–42] while informative, cannot elucidate the structures and pathology unique to the human retina. The small number
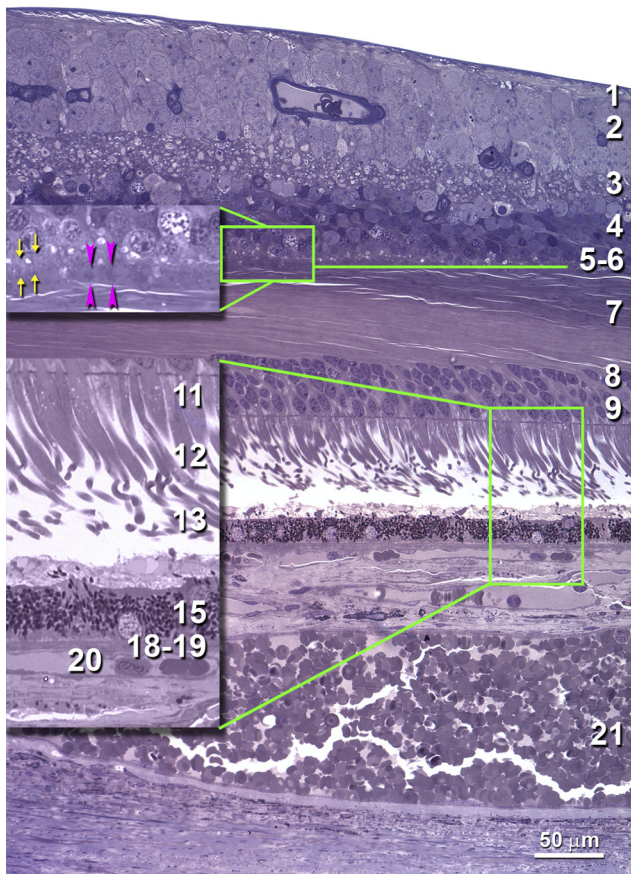
**FIGURE 1.** Chorioretinal layers in a normal human macula. An 0.8-$\mu$m-thick section, toluidine blue, 66-year-old male donor, 1.0 to 1.5 mm nasal to the fovea (see Fig. 3 for complete section). Twenty-one layers, sublayers, and potential spaces[1,4] were identified (*layers enlarged in the *green* frames): (1) NFL; (2) GCL; (3) IPL; (4) INL; (5) OPL, synaptic (OPLsyn, *yellow arrows*); (6) OPL, pedicles (OPLped, *pink arrowheads*); (7) OPLHenle; (8) ONL, rods; (9) ONL, cones; (10) ONL, inner fibers (not present); (11) *inner segments, myoid (ISmy); (12) *inner segments, ellipsoid (ISel); (13) *outer segments; (14) *subretinal drusenoid debris (none present); (15) *retinal pigment epithelium; (16) *BlamD (none present); (17) *lipid wall/ basal linear deposit/ drusen (none present); (18) *inner Bruch's membrane; (19) *outer Bruch's membrane; (20) *choriocapillaris; and (21) choroid. Our definition of OPL subzones differs from that of Polyak,[1] who referred to OPLsyn as plexiform and included rod spherules with cone pedicles in the middle OPL sublayer. We focused on cone pedicles because cones are more abundant in the macula, and their pedicles form a monolayer.[5,6]

of human eyes examined in service of validating OCT[43–46] have included few pathologic specimens, nonmacular tissues, few or poorly specified macular locations, or low-resolution OCT images.

Proper understanding of normal macular layers sets the stage for interpreting abnormalities in disease. We sought to provide a comprehensive set of histologic chorioretinal layer thicknesses at well-specified locations in normal maculas to serve as a reference for clinical OCT and to lay a foundation for future studies of AMD eyes. Toward these goals, we generated 0.8-$\mu$m-thick, macula-wide sections for high-resolution light microscopy, to provide a tissue view comparable to that of an OCT scan, measured layer thicknesses at standard locations, and determined processing-associated tissue volume changes. Because OCT bands and histologic layers vary predictably across the normal macula, plots of histologic laminar boundaries could disclose shape differences indicating discrepancies in

layer assignment. Here, we report thicknesses, laminar boundaries, and age changes for two-layer pairs with historically combined OCT signals: GCL-IPL and OPLHenle-ONL.

## METHODS

### Overview

We measured thicknesses of 21 chorioretinal layers at standard locations in sections through the foveas of 18 human eyes. For 10 of these eyes, ex vivo SD-OCT was used to determine tissue volume changes due to processing of the neurosensory retina. Histologic layer thicknesses, averaged across the 18 maculas, were used to compute laminar boundaries. Boundaries were plotted and compared with representative in vivo SD-OCT images obtained from other eyes.

### Eyes

The University of Alabama Birmingham (UAB) Institutional Review Board approved use of human tissues for this project (X090716009), and the protocols adhered to the Declaration of Helsinki. Eyes preserved by immersion in 1% paraformaldehyde and 2.5% glutaraldehyde in 0.1 M phosphate buffer were withdrawn from a research repository of nondiabetic donor eyes. The median interval between death and preservation was 2:41 hours (range, 57 minutes to 4 hours 51 minutes). Eyes with grossly normal maculas from 40 donors were processed as described below. After specimens with poor embedding, inadequately preserved foveal structure, or mechanical damage were eliminated, 18 eyes remained for analysis (40M, 44F, 51F, 52M, 54M, 57M, 57M, 65M, 66M, 71M, 73F, 76F, 80F, 83M, 84F, 85F, 88F, and 92F; all Caucasian).

### Ex Vivo OCT for Tissue Volume Determination

We determined processing-related tissue volume changes by comparing retinal thickness measured from ex vivo OCT scans of excised macula before histologic processing to thickness measured from sections. Full-thickness eye wall punches centered on the fovea were excised with an 8.25-mm diameter trephine (Surgistar, Knoxville TN). We used a spectral domain OCT system (Spectralis HRA+OCT; software version 5.1.4; Heidelberg Engineering, Heidelberg Germany) with a broadband superluminescent diode at $\lambda$ of 870 nm as a low-coherence light source. Optical depth resolution was ~7 $\mu$m with
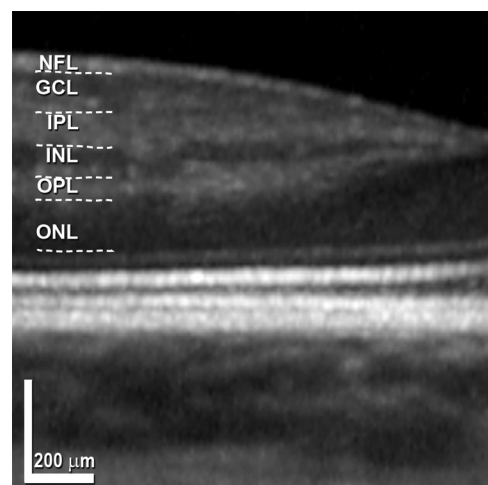


**FIGURE 2.** Layer designations in in vivo SD-OCT. Terminology adapted from References 16, 26–28. Nasal to the fovea in a representative scan, expanded 51% axially. The entire scan, from a 28-year-old woman, is shown in Figure 6A. *Dotted lines*: manual segmentation of the bands for illustrative purposes. NFL, nerve fiber layer; GCL, ganglion cell layer; IPL, inner plexiform layer; INL, inner nuclear layer; OPL, outer plexiform layer; ONL, outer nuclear layer. Scale bracket, 200 $\mu$m vertically and horizontally.

digital resolution reaching 3.5 $\mu$m.[17] Tissue was held in a closed, fluid-filled chamber with a +60-D lens mounted in one vertical side (from Heidelberg Engineering). Macular punches were sutured at four points through the sclera (7-0 curved Vicryl; Ethicon, Somerville, NJ) to an anodized aluminum plate with a circular opening that accommodated scleral curvature and the optic nerve. The plate was held vertically in a slot within the chamber, so that the vitreal surface of the excised macula faced into the machine. We performed horizontal scans through the fovea and optic nerve and volume renditions including 30° slices 60 $\mu$m apart. Signal strength at 28 to 30 dB provided the lowest background noise. Ten B-scans were averaged for each image. The resulting images were exported in tagged image file format (16-bit, 2560 $\times$ 1636 pixels) and composited (Photoshop CS2; Adobe Systems, San Jose CA).

## Tissue Processing

Macular punches were processed by the osmium and paraphenylenediamine (OTAP) method to preserve lipid-rich extracellular AMD-specific lesions[47,48] and with sclera attached to anchor softer tissues. Scleral thickness was reduced 50% to 70% with a scalpel blade to facilitate reagent penetration. Tissues were postfixed in 1% $OsO_4$ 0.1 M in Sorenson's buffer for 2.5 hours (dark, room temperature) with 6 minutes of cyclical push-processing in a microwave oven (Ted Pella, Redding CA), followed by 30 minutes in 1% tannic acid (gallotannin), a 50% acetonitrile wash (ACTN; EMS, Hatfield PA), and fresh paraphenylenediamine in 70% ACTN for 30 minutes. Dehydration steps with increasing ACTN concentrations were also push processed. To improve resin infiltration (EMBed 812; EMS), we used the catalyst benzyldimethylamine (EMS) and kept tissue on a rotating wheel for 3 days, replacing the resin three times. Tissues were cured in labeled flat embedding molds (Ted Pella) for 24 hours at 70°C. Sections were cut at 0.8-$\mu$m thickness (Diatome Histo knife, 6-mm edge; EMS) into a reservoir of deionized water, warmed by proximity to a soldering iron to remove compression, placed on gelatin subbed slides (SLD01-BX; Southern Biotechnology, Birmingham, AL), and dried at 40°C. The slides were stained with 2% toluidine blue O and 2% sodium borohydride at 80°C for 5 minutes, rinsed, dried, cleared in xylene, and coverslipped (Permount; Fisher Scientific, Pittsburgh, PA). Progress through the tissue block was monitored by visualizing the foveal pit under a dissecting scope.

## Layer Thickness Measurements in Histologic Sections

We measured the thicknesses of 21 chorioretinal layers at 25 standard locations, nasal and temporal to the foveal center (systematic sampling, Fig. 3). More locations were analyzed near the fovea, where retinal cell populations change rapidly. From individual layer thicknesses, cumulative thicknesses relative to the RPE basal lamina were determined. From cumulative thicknesses and distances from the fovea (eccentricities), boundaries of the layers were computed. This approach differs from that commonly used by segmentation software for OCT instru-

ments, which detects contrast boundaries between hyper- and hyporeflective layers[49] and calculates thicknesses between the boundaries.

We used a microscope with a 40 $\times$ 0.70 NA plan fluor objective (Eclipse; Nikon, Melville NY), a programmable stepper motor stage with 2 $\mu$m accuracy (BioPoint 2; Ludl Electronics, Hawthorne, NY), a CCD camera (Retiga 4000R; Qimaging, Burnaby, BC, Canada), and software for camera control and morphometry (IP Laboratory, v. 3.9.3r4; Biovision, Exton, PA). The foveal center was assigned by examining stepped sections for GCL and INL gaps, Henle fibers in longitudinal rather than cross-sectional profile,[50] a central ONL lacking rod nuclei, and markers for central bouquet cones (distinctive chromatin, thin inner segments, and long inner fibers). If several sections met these criteria, the one with the largest GCL and INL gaps was designated as the center. Zero on the stage coordinate system was assigned to the foveal center ELM, with an ocular reticule and cross hair.

At each location, images oriented with the NFL on top were viewed at 680$\times$ monitor magnification to measure larger structures and at 1425$\times$ for smaller structures (Fig. 1, insets). Thicknesses perpendicular to the RPE basal lamina were measured starting at the NFL at each location, using the lengths tool and a programmable trackball in a commercial image analysis program (IPLab; Scanalytics, Fairfax, VA). To minimize cumulative errors, each new layer's measurement was started at the previous layer's termination. In these thin sections, the boundaries of nuclear layers undulated around individual cell bodies, and the observer estimated an enveloping boundary. Only continuous layers were measured. Where ganglion cell bodies (GCL), cones pedicles (OPL), and cone nuclei (ONL) were noncontiguous, layer thickness was 0. Only photoreceptor IS in a picket fence configuration were measured, using the longest and straightest myeloid, ellipsoid, and OS available for cones at each location. Retinal detachments were digitally approximated by restarting layer thickness measurements on the other side of the detachment. Measurements were populated into a spreadsheet template (Excel ver. 11.5.6; Microsoft, Redmond WA).

Nonmeasurable locations were treated as missing and assigned $-1$. Because of differences in initial trephining, measurements were made in fewer eyes at 3 mm eccentricity than at more central locations. Measurements were made at all locations <1 mm eccentricity (i.e., fovea) in 8 of 18 eyes. The number of eyes with thickness measurements varied for individual layers as follows: BrM, ChC, and choroid, 18 eyes; layers internal to the ELM, $\geq$16 eyes; IS myeloid and IS ellipsoid, 9 to 18 eyes at different locations; and OS, 1 to 8 eyes. Retinal detachment and thin sections together caused off-axis sectioning and fewer thickness measurements for delicate IS and OS.

## Analysis of Layer Thickness

Thickness measurements were exported in .csv format. Custom programs written in Java were used to organize and analyze data graphically. Thicknesses were interpolated to replace missing values. Cumulative thicknesses relative to the RPE basal lamina computed for retina



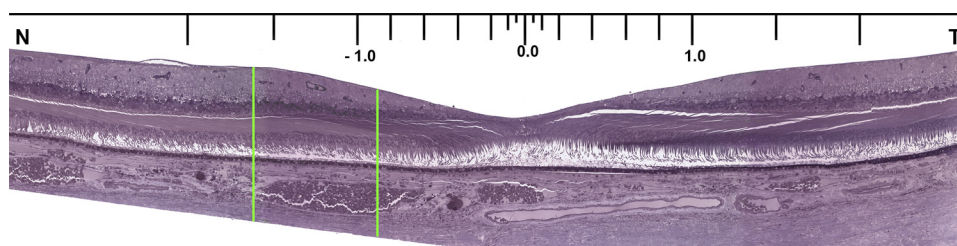**FIGURE 3.** Macular cross section with measurement locations. Thicknesses of layers were measured at standard locations (0.0, 0.05, 0.1, 0.2, 0.4, 0.6, 0.8, 1.0, 1.5, 2.0, 2.5, and 3.0 mm nasal and temporal from the foveal center, as defined by laminar and cytologic criteria). Not all sections included the most eccentric locations due to variability in trephining, including this section. Green lines delimit the area shown in Figure 1.
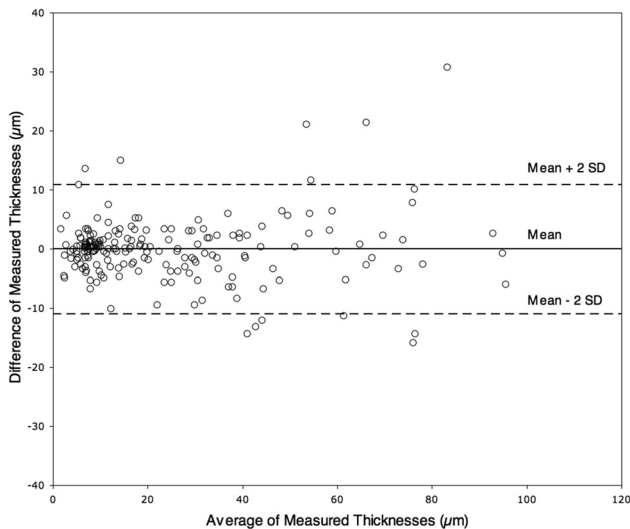
**FIGURE 4.** Interobserver variability in layer thicknesses. Bland-Altman comparison of 195 retinal layer thickness measurements made by two observers (CAC, AM). *Dashed lines*: mean difference ±2 SD; 93.3% (*n* = 182) of the data points fall within the lines. The 13 outliers are discussed in the text.

and for choroid (boundaries) were plotted as positive and negative, respectively. Other programs averaged laminar boundaries or computed other variables at standard locations across eyes.

## Statistical Analysis

One observer (CAC) made all thickness determinations (>9000 total). To validate layer identification and thickness measurements, a second observer (AM) was trained to analyze one image at 1.0 to 3.0 mm nasal containing all retinal layers from each eye. Between-observer differences for each layer's thickness were plotted against average thickness (Bland-Altman plot).[51] The slope of the plot's best-fitting line was determined with linear regression. Individual thickness differences >2 SD were adjudicated openly. Between-observer differences from all eyes (*n* = 195), individual eyes, and individual layers were tested for significance with paired *t*-tests. The criterion significance level of $\alpha =$ 0.05 was corrected for multiple comparisons by the Bonferroni method (*n* = 29 tests; $\alpha = 0.00179$).

A mixed model repeated measures analysis of variance was used to evaluate the association between layer thickness and age. The mixed model allows for the incorporation of both within- and between-subjects effects without the loss of subjects with incomplete data. It also allows for more flexibility in the modeling of the cluster-related correlation structure.

## Representative In Vivo OCT

Histologic chorioretinal layer thicknesses in a composite of the 18 eyes were compared to representative SD-OCT scans of normal macula (obtained with Spectralis HRA+OCT; Heidelberg Engineering). One hundred averaged 30° scans were acquired using eye-tracking and enhanced depth imaging OCT.[20] In the past, such scans were obtained by taking images with the instrument pushed close enough to the eye to create an inverted image, but this feature later was incorporated as a user-selectable software feature. Bands of different reflectivity were manually segmented by authors CAC and JDM (Illustrator; Adobe, San Jose, CA), with reference to previous SD-OCT publications.[52,53] Use of in vivo OCT scans was approved by institutional review (Western IRB, Olympia, WA).

## RESULTS

### Validation of Histologic Layer Thickness Measurements

There was no overall systematic bias in 195 thicknesses measured from sections by two observers, as a regression line through a Bland Altman plot (Fig. 4) did not differ significantly from a line with 0 slope. Discrepancies between observers for 13 of 195 measurements were attributed to nonsystematic reasons, including differences in measurement locations, interpretation of layer continuity, compensating for discrepancies in adjacent layers, differing angle of measuring line across the retina, and inadequate stain contrast between INL and IPL. No significant differences between observers were discerned either for measurements within individual eyes or within specific layers across eyes (*P* > 0.0017, Bonferroni corrected). Absent systematic differences with a second observer, the first observer's measurements were used for subsequent analyses.

### Processing-Related Tissue Volume Change

In 10 of 18 sectioned eyes, we assessed changes in tissue volume due to processing after eye preservation in ex vivo OCT (Fig. 5A). The distance from ILM to inner RPE (total retinal thickness) was determined at the same nominal distances from the foveal center as in subsequent histologic sections through the same retinas. Only neurosensory retina was analyzed, because NFL and RPE inner boundaries were clear by ex vivo OCT, and the choroid–sclera boundary was not. Total retinal thickness in ex vivo OCT and histology were plotted, and differences in the areas under the two curves were computed. This analysis revealed several points. First, in these 10 eyes, the shape and extent of the foveal depression by histology corresponded well with its shape in ex vivo OCT (Fig. 5B). Second, the median area difference between thickness curves for ex vivo OCT and histology was 14.5% (range, 4.0%–39.0%). Third, differences at the foveal center were greater (median, 29.5%; range, 17.0%–65.0%) than elsewhere. Shrinkage was not con-
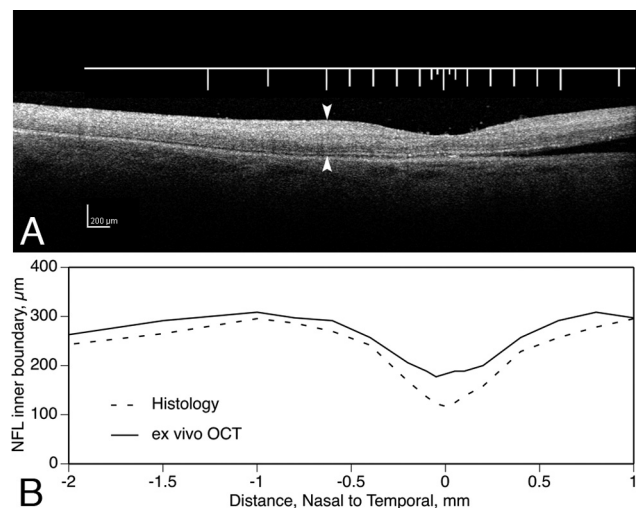


**FIGURE 5.** Processing-related tissue volume changes. (**A**) Ex vivo OCT image of a normal macula (66-year-old male donor), preserved in glutaraldehyde and paraformaldehyde, excised, and viewed by SD-OCT (Spectralis HRA+OCT; Heidelberg Engineering). The ruler shows locations where total retinal thickness from NFL to RPE was also measured. These locations were nominally the same used in histologic measurements of the same eye. (**B**) Total retinal thickness determined from the ex vivo SD-OCT scan in (**A**) and from a histologic section through the foveal center. Thickness of this retina decreased in processing 9.0% overall, 33.0% at the foveal center.

sistently related to the death-to-preservation interval. We chose not to correct thickness measurements for these tissue volume changes, because we could not apply corrections to all eyes in the study, and we cannot yet correct measurements from the choroid. Further, the retinal volume changes revealed by ex vivo OCT are not well characterized. Edema is microscopically detectable in postmortem specimens, and the retina can thicken transiently after arterial occlusion in vivo.[54] Thus, retinal thicknesses determined from ex vivo OCT, may overestimate both true thickness and true shrinkage.

Table 1 shows the mean thicknesses of chorioretinal layers in micrometers and as a percentage of retina or choroid. The greatest contributors to total retinal thickness at 1 mm are the GCL, INL, and OPLHenle and, at the foveal center, OPLHenle, ONL cones, and OS. Standard deviations (SDs) varied among layers and were greater for total choroid (SD/mean = 35.1% at foveal center, 43.4%-44.0% at 1 mm) than for total retina (SD/mean = 34.4% at foveal center; 11.8%-14.7% at 1 mm). Variability was not related to the donor's sex. Variability related to aging is described below.

## Comparison of Histologic Layers to Representative In Vivo SD-OCT

Figures 6A and 6B show chorioretinal layers in normal macula at a fivefold expanded vertical scale for a representative SD-OCT scan and average histologic layer thickness determined in the 18 sectioned eyes. By comparing the shapes of bands and layers in a common format, similarities and differences are readily discerned. Both representations show a correspondence in overall shape, a thickening of the NFL close to the optic nerve head, an outward bowing of the choroid, and a choroid that is thinner nasally than temporally.[55] In contrast, histologic layers are overall thin relative to their OCT counterparts, especially at the foveal center, where the relative thinness makes the pit look artificially deep. Nasotemporal differ-

ences within the central macula are less apparent in the OCT scan, in part because GCL and IPL bands are merged.

Finer-grain differences between OCT bands and histologically defined layers are emphasized by arrowheads in Figures 6A and 6B. First, the hyperreflective OPL band is thin and bends inwardly to form a singular promontory at the foveal center (Fig. 6A, pink). The histologic OPL is thick and complex, bending inward outside the foveal center and then outward at the very center (pink, Fig. 6B). This difference is due to greater tissue shrinkage at the foveal center, but not entirely, as other layers are not affected similarly at that location. Another potential contributor is that some sectioned foveas included in these mean thickness data have a very thin ONL in the foveal center.[1] Such a finding may escape detection between the scans of an OCT volume rendition, like our Figure 6A. Second, a hyporeflective ONL band exhibits a large and distinct inward bend at the fovea (Figs. 6A, 6B, green). Third, the ONL band visible by OCT occupies a greater proportion of total retinal thickness than does the histologic ONL, because it includes both the histologic ONL and OPLHenle (Figs. 6A, 6B, yellow). Conversely, the OPL band in OCT is thinner than the histologic OPL, because it does not include the Henle fiber component.

## Description of GCL-IPL and OPLHenle-ONL

Here, we describe pairs of histologic layers (GCL+IPL, OPLHenle+ONL) that can produce combined signals in OCT, using average thickness data from the 18 sectioned eyes (Figs. 7, 8). The GCL rises to maximum thickness at 0.8 to 1 mm eccentricity (72.8 $\mu$m, nasal, 59.3 $\mu$m temporal) and decreases to 13.8 to 19.6 $\mu$m at 3 mm eccentricity (Figs. 7A, 7B). In contrast, the IPL is thickest (38.5 $\mu$m) farther out (1.5 mm, Figs. 7A, 7C) and thins little with greater eccentricity. These differing eccentricity dependencies of the GCL and IPL create a complex relationship for the percentage of the combined GCL+IPL band

**TABLE 1.** Layer Thicknesses Measured in Histologic Sections of 18 Maculas

| Layer | Nasal, 1 mm | | | Fovea Center | | | Temporal, 1 mm | | |
|---|---|---|---|---|---|---|---|---|---|
| | Mean | SD | % of Total | Mean | SD | % of Total | Mean | SD | % of Total |
| 1. NFL | 18.4 | 6.4 | 5.3 | 0.0 | 0.0 | 0.0 | 11.1 | 9.0 | 3.4 |
| 2. GCL | 72.8 | 23.1 | 21.1 | 0.0 | 0.0 | 0.0 | 56.7 | 12.7 | 17.3 |
| 3. IPL | 36.9 | 8.9 | 10.7 | 0.0 | 0.0 | 0.0 | 35.3 | 6.1 | 10.7 |
| 4. INL | 63.9 | 10.2 | 18.5 | 0.0 | 0.0 | 0.0 | 59.1 | 11.9 | 18.0 |
| 5. OPLsyn | 6.7 | 2.0 | 1.9 | 0.0 | 0.0 | 0.0 | 6.8 | 2.0 | 2.1 |
| 6. OPLped | 7.1 | 2.2 | 2.0 | 0.0 | 0.0 | 0.0 | 6.1 | 2.2 | 1.8 |
| 7. OPLHenle | 48.9 | 17.1 | 14.2 | 21.6 | 12.8 | 14.7 | 54.5 | 19.8 | 16.6 |
| 8. ONL, rods | 18.3 | 5.7 | 5.3 | 0.0 | 0.0 | 0.0 | 20.7 | 4.3 | 6.3 |
| 9. ONL, cones | 10.3 | 3.1 | 3.0 | 33.6 | 13.9 | 22.9 | 11.3 | 2.8 | 3.4 |
| 10. ONL, inner fibers | 0.0 | 0.0 | 0.0 | 19.9 | 8.6 | 13.6 | 0.0 | 0.0 | 0.0 |
| 11. ISmy | 9.5 | 2.9 | 2.8 | 8.1 | 2.8 | 5.5 | 9.1 | 2.9 | 2.8 |
| 12. ISel | 15.9 | 4.5 | 4.6 | 20.9 | 3.0 | 14.3 | 15.1 | 2.8 | 4.6 |
| 13. OS | 21.9 | 7.7 | 6.4 | 28.4 | 5.2 | 19.4 | 28.1 | 10.1 | 8.6 |
| 14. Subretinal drusenoid debris | 0.0 | 0.0 | 0.0 | 0.0 | 0.0 | 0.0 | 0.0 | 0.0 | 0.0 |
| 15. Retinal pigment epithelium | 14.0 | 2.9 | 4.1 | 14.1 | 3.9 | 9.6 | 13.5 | 2.1 | 4.1 |
| 16. Basal laminar deposit | 0.0 | 0.0 | 0.0 | 0.0 | 0.0 | 0.0 | 0.0 | 0.0 | 0.0 |
| 17. Lipid wall/basal linear deposit/drusen | 0.0 | 0.0 | 0.0 | 0.0 | 0.0 | 0.0 | 0.0 | 0.0 | 0.0 |
| 18. Inner Bruch's membrane | 1.7 | 0.5 | 1.7 | 1.9 | 0.6 | 1.5 | 1.7 | 0.5 | 1.4 |
| 19. Outer Bruch's membrane | 2.5 | 1.0 | 2.4 | 2.8 | 0.9 | 2.2 | 2.4 | 1.0 | 1.9 |
| 20. Choriocapillaris | 5.1 | 1.1 | 4.9 | 6.8 | 2.5 | 5.4 | 5.2 | 2.0 | 4.2 |
| 21. Choroid | 95.2 | 44.3 | 91.1 | 114.2 | 44.0 | 90.9 | 115.0 | 54.1 | 92.5 |
| Total, neurosensory retina (1–16) | 336.6 | 49.6 | | 158.8 | 54.6 | | 323.6 | 38.0 | |
| Total, choroid (17–21) | 104.5 | 45.4 | | 125.7 | 44.1 | | 124.3 | 54.7 | |
| Total | 441.1 | | | 284.5 | | | 447.9 | | |

Values were set to 0 where SD > mean. These include the GCL, IPL, INL, OPLsyn, and OPLped at the foveal center; ONL inner fibers at 1 mm nasal and temporal; and subretinal drusenoid debris, basal laminar deposit, and lipid wall/basal linear deposit throughout. The percentage of total thickness was calculated for layers 1 to 16 (neurosensory retina) and 17 to 21 (choroid).
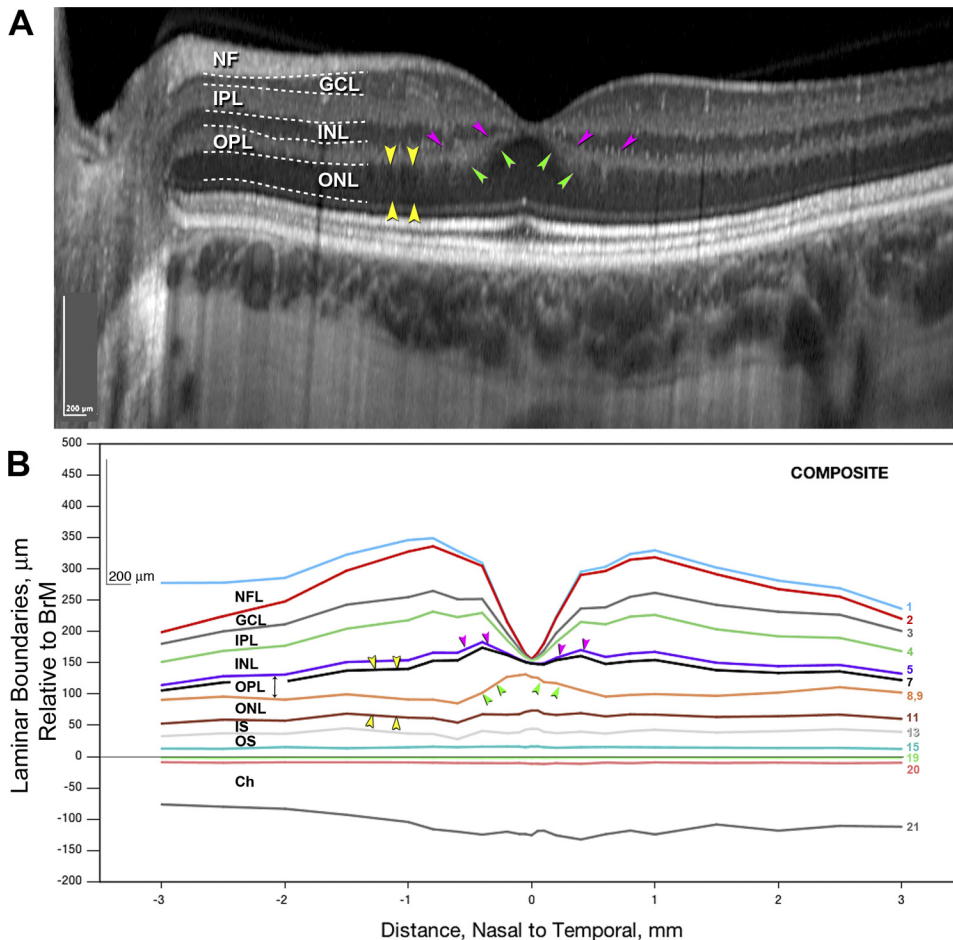
FIGURE 6. Chorioretinal layers in normal macula. Representative in vivo SD-OCT scan (**A**) and composite histologic layers (**B**) are shown at fivefold expanded axial scale to enhance layer shape differences. (**A**) Normal macula in a 28-year-old woman (100 SD-OCT scans with extended depth imaging were averaged; see also Fig. 2). Bands were manually segmented (*dotted lines*) for illustrative purposes. (**B**) Histologic laminar boundaries were computed from average layer thicknesses in sections of 18 maculas. Boundaries are referenced to the RPE basal lamina of BrM, with the neurosensory retina as positive and the choroid as negative on the *y*-axis. The boundaries are traceable to histologic layers in Figure 1 by numbers at the right. Some numbers are absent, because thin layers were combined (ISmy and ISel, inner and outer BrM) or omitted (OPLped) for illustrative clarity. All OPL components are shown in Figure 8. Other missing numbers represent essentially absent layers (see note to Table 1). Letter labels indicate the nine thickest layers. (**A**, **B**, *pink arrowheads*) A Hyperreflective OPL band bends inward and the histologic OPL bends outward. (**A**, **B**, *green arrowheads*) Hyporeflective ONL band, which occupies a greater proportion of total retinal thickness than the histologic ONL. (**A**, **B**, *yellow arrowheads*) Hyporeflective ONL band includes both ONL and OPLHenle.

occupied by each of these components (Fig. 7D). At 0.4 to 0.6 mm eccentricity, GCL occupies 70.7% of the combined band, declining to equality with IPL at 2 mm and decreasing to 38.9% to 44.0% at the macular edge.

Similar considerations cause us to apportion differently the macular volume currently attributed to OPL and ONL (Fig. 8). The two OPL sublayers, called synaptic and pedicles,[1] first appear at the 0.4-mm measurement location, then they are 5 to 6 $\mu$m thick until the cone pedicle monolayer breaks up at >2 mm eccentricity (Fig. 8A). The hyporeflective OCT band called the ONL comprises two distinct layers. Innermost is OPLHenle (Fig. 8B), which rises to a maximum thickness at 0.4 mm eccentricity (72.0 $\mu$m nasal and 54.6 $\mu$m temporal) and declines from there to 13.5 to 20.0 $\mu$m at the macular edge. The outermost component of the OCT band called the ONL is the true ONL (Fig. 8C). This layer is thickest (62.2 $\mu$m) in an inward bulge at the foveal center and thins to 30.7 to 36.6 $\mu$m at 0.4 to 0.5 mm eccentricity. It slowly increases to 41.9 $\mu$m temporally and 38.1 $\mu$m nasally, before a peripapillary decline. Percentages of the OCT band occupied by OPLHenle and ONL show a complex eccentricity dependency (Fig. 8D). ONL occupies >60% of the combined layer within 0.2 mm eccentricity. OPLHenle occupies almost 70% at 0.6 to 1.5 mm eccentricity, where the Henle fibers are longest. ONL resumes a predominant proportion at higher eccentricities, as the OPL-Henle thickness dwindles.

### Aging Changes in Chorioretinal Layer Thickness

No significant differences between donors <70 years of age and those aged >70 years were detected in total thickness of the neurosensory retina (layers 1–16). Significant age differences in thickness were detected for 5 of the 21 individual layers, of which the three most robust are shown in Figure 9. RPE was 17.1% thinner in older eyes (2.5 $\mu$m, $P < 0.004$; Fig. 9B). The choroid thinned more markedly (29.6%, 35.6 $\mu$m, $P < 0.05$, Fig. 9C), principally because five of the thinnest choroids were found among older donors. Unexpectedly, OPLHenle thickened with age ($P < 0.04$, Fig. 9A), becoming 20.8% thicker in the older eyes than in the younger ones. The results for two other layers, while statistically significant, are considered less robust (not shown). In a smaller number of eyes with IS measurements, IS ellipsoid was 10.8% (2.0 $\mu$m) thinner in older eyes. BlamD, absent in seven of nine eyes <70 years and three of nine eyes >70 years, had high variance measurements due to its patchiness.

### DISCUSSION

Motivated by the widespread use of clinical OCT, we sought to provide a device-independent description of the histologic chorioretinal layers as a reference for this rapidly evolving technology. We generated the first graphic representation and database of absolute and proportional thicknesses for 21 chorioretinal layers across the macula. Our approach capitalized on marked topographic changes in macular layers, to compare histology and OCT scans from different eyes intuitively, using a common format. Because regional differences in macular cytology exhibit radial symmetry around the foveal center,[31,50,56] we localized thicknesses in units of distance from this landmark, unlike studies using small macular samples.[21,44] From thickness measure-
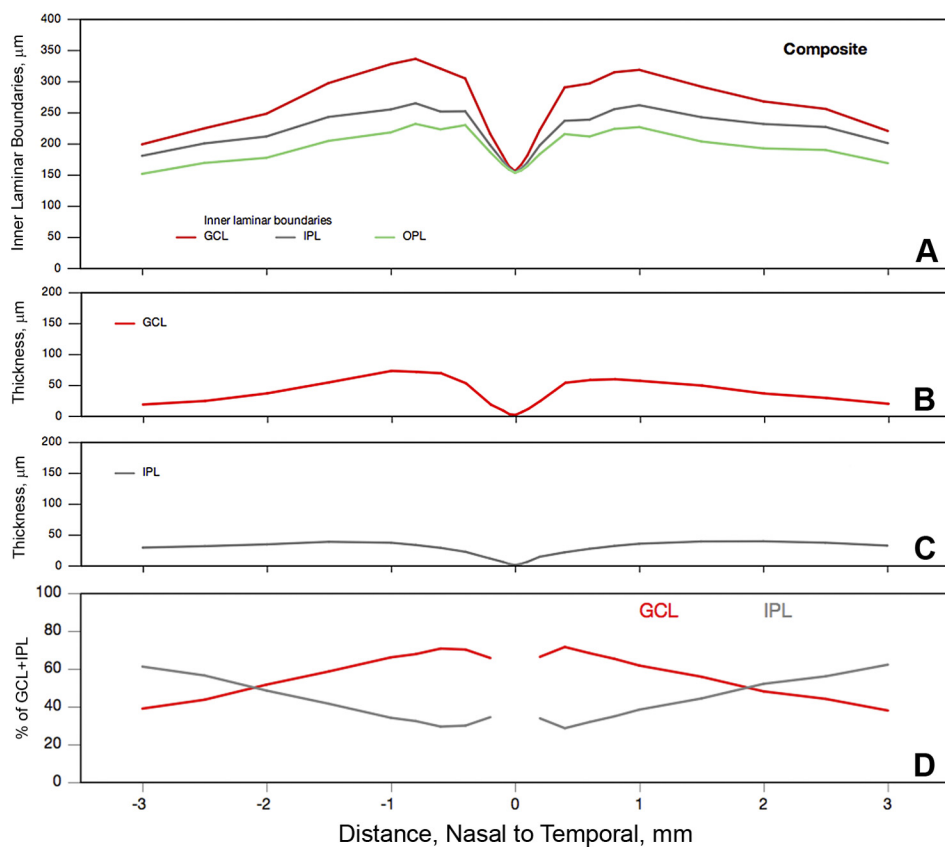
**FIGURE 7.** GCL and IPL boundaries, thicknesses, and relationships. Average layer thicknesses were determined from 18 histologically sectioned maculas. (**A**) Inner laminar boundaries (cumulative thickness relative to RPE basal lamina). (**B**) Thickness of the GCL. (**C**) Thickness of the IPL. (**D**) Percentage of the combined GCL-IPL occupied by individual layers.
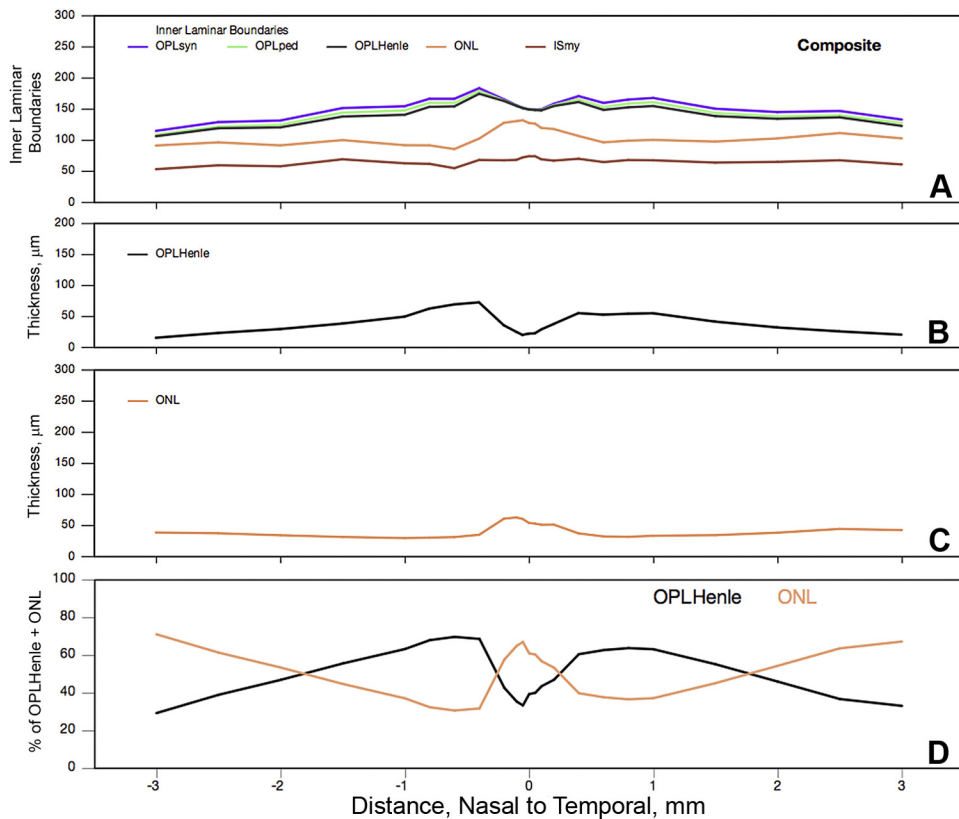


**FIGURE 8.** OPL and ONL boundaries, thicknesses, and relationships. Average layer thicknesses were determined from 18 histologically sectioned maculas. (**A**) Inner laminar boundaries (cumulative thickness relative to RPE basal lamina). (**B**) Thickness of OPL components. (**C**) Thickness of ONL. (**D**) Percentage of combined OPLHenle+ONL occupied by individual layers.
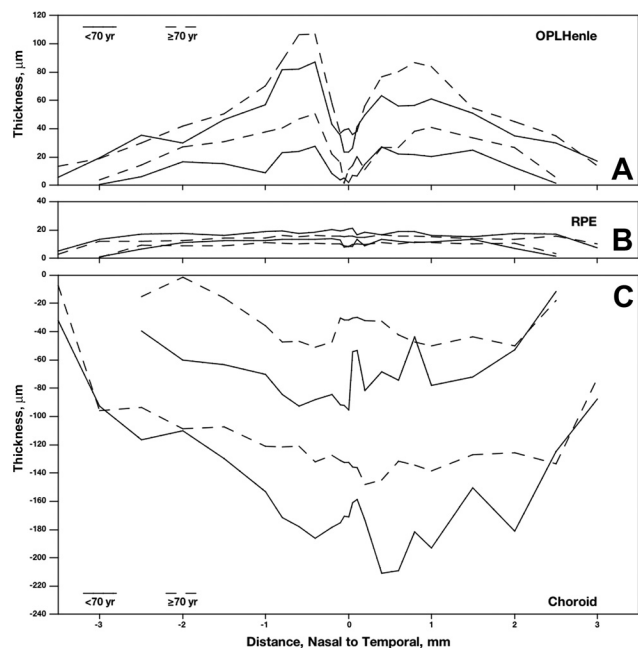
**FIGURE 9.** Age-effects in chorioretinal layers. Layer thicknesses and boundaries were determined in 18 sectioned maculas, age 40 to 92 years. Three of 21 layers showed significant and robust differences between donors <70 years and donors ≥70 years of age. Two lines for each age group show confidence limits. **(A)** OPLHenle was thicker in older eyes. **(B, C)** The RPE and choroid were thinner in older eyes.

ments and laminar boundaries for two-layer pairs for which signals are commonly combined in OCT scans, we detected an age-related increase in thickness specific to OPLHenle with potential mechanistic implications for Müller cell biology.

## METHODOLOGICAL CONSIDERATIONS: TISSUE PREPARATION AND ANALYSIS

This study can be compared to that of Anger et al.,[31] who determined laminar boundaries in ex vivo OCT scans and macula-wide, semithin sections of the same perfused monkey retinas (Table 2). Unlike Anger et al.,[31] we used ex vivo OCT for overall shrinkage assessment only,[31,42] and we eschewed the longitudinal reflectance profile (LRP) for analysis. The LRP displays variation in reflectance along a single vertical line across the retina and is well suited for establishing layer presence, locating layer boundaries, and quantifying local contrast.[30,38,42] While the LRP circumvents subjective methods relying on visual judgments, its use for layer designation requires matching of retinal location, plus assumptions about the correspondence of layers and OCT bands for proper vertical scaling and accurate assessment of layer-specific tissue volume changes.[41] In contrast, we showed regional differences in layer thickness independent of scaling.

Our tissue preparation method was chosen with a longer-term goal of providing a database of layer thicknesses in eyes at different stages of AMD. Because the neural retina and vascular choroid differ substantially in their cellular and extracellular components and the thickness of their constituent layers, no single tissue preparation method is ideal for all layers. We chose a modified electron microscopy protocol to preserve lipid-rich extracellular lesions in the sub-RPE space[57,58] that are not yet well resolved by OCT. This protocol will allow separation of basal deposits and better overall light microscopic morphology[59] than either thicker paraffin-embedded (4–7 $\mu$m)[60–62] or cryosections (7–12 $\mu$m).[63] Other OCT–histology comparisons used cryostat sections,[24,38,64] to reduce tissue volume changes inherent to dehydration with organic solvents, with the disadvantage of reduced resolution in thicker sections. Our tissue volume changes (median, 14.5%), while not negligible, are nevertheless comparable with those in previous reports of 40% to 50%.[23,31,42] Limitations to our method include the use of archival tissues initially preserved several hours after death and inconsistent visualization of the OS–RPE interface. Our planned studies of correlates to the outer retinal hyperreflective bands will therefore incorporate additional methods to examine that interface specifically.

It is difficult to directly compare our histologic thicknesses measured along a single plane with those reported for ETDRS zones by software used with current SD-OCT instruments. Further, this software varies in the number of layers included in retinal thickness determination.[65] Nonetheless, our mean retinal thickness of 158 $\mu$m for the foveal

**TABLE 2.** Comparison of the Present Study and Anger et al.[31]

| Parameter | Present Study | Anger et al.[31] |
| --- | --- | --- |
| Species | Human | M. Fascicularis monkey |
| Purpose of study | Layer thicknesses | Band-layer correspondence |
| Number of samples | 18 | 8 |
| OCT | Ex vivo SD-OCT, for shrinkage estimation; representative clinical SD-OCT images | Ex vivo, ultra-high resolution, for definition of reflective bands |
| OCT-histology correlation | Compared to unmatched eyes | Compared to same eyes |
| Death to preservation, h | <4 | ~0 |
| 1° fixation method | Immersion | Perfusion |
| 1° fixative | 2% glutaraldehyde, 1% paraformaldehyde, phosphate buffer | 4% paraformaldehyde, phosphate buffer |
| Time to processing | Extended | Not mentioned |
| Postfixation | Osmium tannic acid paraphenylenediamine | None |
| Section thickness | 0.8 $\mu$m | Semithin |
| Stain | Toluidine blue (all tissue) | Methylene blue (nuclei) |
| Layers studied | Chorioretinal | Retina |
| Shrinkage assessment | Total retinal thickness | Layer by layer |
| Handling of processing-related distortion of retinal layers | Normalization of thicknesses to an arbitrary 0 line (RPE basal lamina) | Geometric normalization of layer boundaries based on OCT scan proportions |
| Henle fibers | Detected by histology only | Detected by OCT and histology (separate figures) |
| Preservation of photoreceptor IS and OS | Variable | Excellent |
| Potential for specimens with disease | Good | Limited |

center (205 $\mu$m corrected for shrinkage) is 8% lower than the 221 $\mu$m reported by patients >40 years imaged with a Spectralis,[66] which calculates thickness for at least layers 1 to 17 and possibly including 18 and 19.[65]

## Macular Neuroanatomy and OCT Interpretation

Our results for layer thicknesses can be compared to previous descriptions of human macula. Around the fovea, inner retinal cells are displaced centrifugally, and photoreceptor IS are compressed centripetally,[1,5,67] resulting in steep gradients of photoreceptor and ganglion cell density and an aster of Henle fibers radiating across the entire macula.[50,68] Our GCL thickness measurements are consistent with descriptions of this layer as six cells deep at its thickest and a monolayer at 3 mm eccentricity.[1,68] The slightly thicker GCL nasal to the foveal center may be due to the nasal retina's ~15% higher GC density.[68] The site of IPL maximum thickness is more eccentric than the GCL maximum, because bipolar cell processes near the fovea travel obliquely to contact GCL neurons.[5,50,69] We found that OPLHenle accounted for 14.2% to 16.6% of total neurosensory retinal thickness at 1 mm eccentricity, similar to both the GCL and INL at this location, underscoring the importance of this distinctive layer for macular physiology. OPL-Henle thickness is due to the length of the individual fibers (600 $\mu$m for cone IS at 0.36–0.40 mm eccentricity[50]), which confer unique biophysical properties on macular photoreceptors.[70]

Older OCT technologies combined signals from adjacent retinal layers in a complex, eccentricity-dependent mix, but newer systems can now disambiguate these layers in vivo. OCT before SD-OCT did not separate the GCL and IPL and not all SD-OCT scans currently show a distinct boundary. However, use of signal averaging to reduce speckle noise and broader band illumination not only separates these layers,[29,30,52] but also reveals IPL sublayers attributable to bipolar synaptic terminals.[71] In humans, 50% of GCs localize to the macula,[68] and reliable methods to separate GCL and IPL by SD-OCT may be valuable for computing the cells remaining at different stages of glaucoma. With regard to OPLHenle, it was recognized that the hyporeflective ONL band included an inner sublayer of contrasting reflectivity consistent with that designation.[16,31] These birefringent fibers[72,73] can now be visualized reliably in OCT by altering the position of light entering through the pupil.[74,75] The shape of OPLHenle in vivo qualitatively resembles our histology-based delineation, and its thickness represents 14.3% to 16.0% of the distance between the inner limiting membrane and the apical RPE surface, compared to 15.2% to 17.6% computed for the same distance in our average eye. Separation of OPLHenle and ONL in SD-OCT may allow more meaningful assessments of photoreceptor number and volume for comparison to acuity measures in the same individuals.

## Differential Aging Effects in Chorioretinal Layers

This study found distinctive, nonuniform effects of aging on individual layers that relate to previous OCT and histologic studies. The choroid and RPE were both thinner in eyes aged >70 years. In vivo, this vascular bed thins ~30% between 20 and 80 years of age[55] and substantially more in age-related choroidal atrophy.[76] Large histologic surveys[77] also report a degree of choroidal thinning through adulthood (38.5%) similar to ours, accompanied by choriocapillaris dropout. Confirmed through both imaging and histology, choroidal thinning must be regarded as a major age change affecting the outer retina. We find a modest (11%) thinning of the aging RPE. This cell, central to AMD pathogenesis, undergoes prominent morphologic and molecular changes during aging.[78] Monolayer thinning redistributes cell volume in a compensatory manner

after RPE loss associated with pathology at extreme ages.[79] The number of macular RPE cells changes minimally during adulthood (studies show no change[80,81]; an increase[82]; or a decrease[83]; reviewed in Ref. 84), not inconsistent with a small degree of thinning. Another possibility is that RPE thinning reflects direct or indirect effects of the choroidal changes. It is hypothesized that reduced blood flow promotes visual dysfunction and the onset of age-related disease,[85] if not via hypoxia in this highly oxygenated vascular bed, perhaps through effects on BrM.[86]

Surprisingly, OPLHenle was 21% thicker in older eyes, countering the common expectation that aging tissues necessarily atrophy. OPLHenle contains processes of photoreceptors and Müller cells,[1] which are closely coupled metabolically and structurally. A key question is which cells are the major contributor to this effect. Throughout adulthood in normal human eyes, 30% of macular rods die, whereas cones remain stable,[87] so we hypothesize that layer thickening is due to an increase in the volume of Müller cells rather than photoreceptor axons. Müller cells respond to numerous acute and chronic insults,[88] including aging,[89–91] by upregulating glial fibrillary acidic protein and intermediate fiber content and by subtly changing their shapes.[92] Whether similar changes occur in the macula is not yet known. However, modeling studies suggest that increased volume of Müller cells and astroglia together partly mask a bona fide age-related decrease in ganglion cell axons in the human NFL,[93,94] a finding with implications for both how NFL layer thicknesses in OCT are interpreted and for the plausibility of Müller cell hypertrophy in OPLHenle. OCT methods that reveal the Henle fiber in vivo[74] may provide insight into these processes, particularly as Müller cells progress to advanced reactivity in AMD.[95]

Limitations of our aging study design include small sample size, lack of information about refractive error in donor eyes,[96] and the necessarily cross-sectional nature of histology. Further, we did not detect a decrease in the peripapillary NFL that is consistently shown by OCT (e.g.,[97]), probably because few eyes had thickness measurements at ≥3.0 mm nasal to the fovea. Perhaps for that reason we did not detect a decrease in overall retinal thickness that is largely accounted for by NFL thinning.[98,99]

## Conclusion

Our ability to recognize and quantify disease states and to understand pathobiology depends critically on knowing the normal anatomic relationships that are increasingly revealed by clinical OCT. We provided the most complete histologic description of chorioretinal layer thicknesses in normal macula to date. These data may inform future inquiries involving these layers in large patient cohorts, as newer OCT technologies disseminate.

### *References*

1. Polyak SL. *The Retina*. Chicago: University of Chicago; 1941.
2. Klein R, Davis MD, Magli YL, Segal P, Klein BEK, Hubbard L. The Wisconsin Age-Related Maculopathy Grading System. *Ophthalmology*. 1991;98:1128–1134.
3. Boycott BB, Dowling JE. Organization of the primate retina: light microscopy. *Phil Trans Roy Soc Lond B*. 1969;255:109–184.

4. Hogan MJ, Alvarado JA, Weddell JE. Histology of the human eye. *An Atlas and Textbook.* Philadelphia: WB Saunders; 1971.

5. Schein SJ. Anatomy of macaque fovea and spatial densities of neurons in foveal representation. *J Comp Neurol.* 1988;269:479–505.

6. Ahnelt PK, Pflug R. Telodendrial contacts between foveolar cone pedicles in the human retina. *Experientia.* 1986;42:298–300.

7. Bressler SB, Bressler NM, Sarks SH, Sarks JP. Age-related macular degeneration: nonneovascular early AMD, intermediate AMD, and geographic atrophy. In: Ryan SJ, ed. *Retina.* St. Louis: Mosby;2006: 1041–1074.

8. Sarks S, Cherepanoff S, Killingsworth M, Sarks J. Relationship of basal laminar deposit and membranous debris to the clinical presentation of early age-related macular degeneration. *Invest Ophthalmol Vis Sci.* 2007;48:968–977.

9. Rudolf M, Malek G, Messinger JD, Wang L, Clark ME, Curcio CA. Sub-retinal drusenoid deposits in human retina: organization and composition. *Exp Eye Res.* 2008;87:402–408.

10. Elman MJ, Aiello LP, Beck RW, et al. Randomized trial evaluating ranibizumab plus prompt or deferred laser or triamcinolone plus prompt laser for diabetic macular edema. *Ophthalmology.* 2010; 117:1064–1077, e35.

11. Diabetic Retinopathy Clinical Research Network. A randomized trial comparing intravitreal triamcinolone acetonide and focal/grid photocoagulation for diabetic macular edema. *Ophthalmology.* 2008;115:1447–1449, e1–e10.

12. Nguyen QD, Shah SM, Heier JS, et al. Primary end point (six months) results of the ranibizumab for edema of the macula in diabetes (READ-2) study. *Ophthalmology.* 2009;116:2175–2181, e1.

13. Spaide RF, Chang LK, Klancnik JM, et al. Prospective study of intravitreal ranibizumab as a treatment for decreased visual acuity secondary to central retinal vein occlusion. *Am J Ophthalmol.* 2009;147:298–306.

14. Campochiaro PA, Heier JS, Feiner L, et al. Ranibizumab for macular edema following branch retinal vein occlusion: six-month primary end point results of a phase III study. *Ophthalmology.* 2010;117: 1102–1112, e1.

15. Khanifar AA, Koreishi AF, Izatt JA, Toth CA. Drusen ultrastructure imaging with spectral domain optical coherence tomography in age-related macular degeneration. *Ophthalmology.* 2008;115: 1883–1890.

16. Drexler W, Sattmann H, Hermann B, et al. Enhanced visualization of macular pathology with the use of ultrahigh-resolution optical coherence tomography. *Arch Ophthalmol.* 2003;121: 695–706.

17. Wolf-Schnurrbusch UE, Enzmann V, Brinkmann CK, Wolf S. Morphologic changes in patients with geographic atrophy assessed with a novel spectral OCT-SLO combination. *Invest Ophthalmol Vis Sci.* 2008;49:3095–3099.

18. Yi K, Mujat M, Park BH, et al. Spectral domain optical coherence tomography for quantitative evaluation of drusen and associated structural changes in non-neovascular age-related macular degeneration. *Br J Ophthalmol.* 2009;93:176–181.

19. Unterhuber A, Povazäy B, Hermann B, Sattmann H, Chavez-Pirson A, Drexler W. In vivo retinal optical coherence tomography at 1040 nm: enhanced penetration into the choroid. *Opt Express.* 2005;13:3252–3258.

20. Spaide RF, Koizumi H, Pozonni MC. Enhanced depth imaging spectral-domain optical coherence tomography. *Am J Ophthalmol.* 2008;146:496–500.

21. Toth CA, Narayan DG, Boppart SA, et al. A comparison of retinal morphology viewed by optical coherence tomography and by light microscopy. *Arch Ophthalmol.* 1997;115:1425–1428.

22. Yabushita H, Bouma BE, Houser SL, et al. Characterization of human atherosclerosis by optical coherence tomography. *Circulation.* 2002;106:1640–1645.

23. Cilingiroglu M, Oh JH, Sugunan B, et al. Detection of vulnerable plaque in a murine model of atherosclerosis with optical coherence tomography. *Catheter Cardiovasc Interv.* 2006;67:915–923.

24. Gambichler T, Moussa G, Regeniter P, et al. Validation of optical coherence tomography in vivo using cryostat histology. *Phys Med Biol.* 2007;52:N75–N85.

25. Drexler W, Fujimoto JG. State-of-the-art retinal optical coherence tomography. *Prog Retin Eye Res.* 2008;27:45–88.

26. Drexler W, Morgner U, Ghanta RK, Kartner FX, Schuman JS, Fujimoto JG. Ultrahigh-resolution ophthalmic optical coherence tomography. *Nat Med.* 2001;7:502–507.

27. Costa RA, Calucci D, Skaf M, et al. Optical coherence tomography 3: automatic delineation of the outer neural retinal boundary and its influence on retinal thickness measurements. *Invest Ophthalmol Vis Sci.* 2004;45:2399–2406.

28. Ko TH, Fujimoto JG, Duker JS, et al. Comparison of ultrahigh- and standard-resolution optical coherence tomography for imaging macular hole pathology and repair. *Ophthalmology.* 2004;111: 2033–2043.

29. Hangai M, Yamamoto M, Sakamoto A, Yoshimura N. Ultrahigh-resolution versus speckle noise-reduction in spectral-domain optical coherence tomography. *Opt Express.* 2009;17:4221–4235.

30. Tanna H, Dubis AM, Ayub N, et al. Retinal imaging using commercial broadband optical coherence tomography. *Br J Ophthalmol.* 2010;94:372–376.

31. Anger EM, Unterhuber A, Hermann B, et al. Ultrahigh resolution optical coherence tomography of the monkey fovea: identification of retinal sublayers by correlation with semithin histology sections. *Exp Eye Res.* 2004;78:1117–1125.

32. Zawadzki RJ, Jones SM, Olivier SS, et al. Adaptive-optics optical coherence tomography for high-resolution and high-speed 3D retinal in vivo imaging. *Opt Express.* 2005;13:8532–8546.

33. Coscas G, Coscas F, Vismara S, Souied E, Soubrane G. Spectral domain OCT in age-related macular degeneration: preliminary results with Spectralis HRA-OCT (in French). *J Fr Ophthalmol.* 2008; 31:353–361.

34. Fernández EJ, Hermann B, Povazay B, et al. Ultrahigh resolution optical coherence tomography and pancorrection for cellular imaging of the living human retina. *Opt Express.* 2008;16:11083–11094.

35. Cucu RG, Podoleanu AG, Rogers JA, Pedro J, Rosen RB. Combined confocal/en face T-scan-based ultrahigh-resolution optical coherence tomography in vivo retinal imaging. *Opt Lett.* 2006;31:1684–1686.

36. Michels S, Pircher M, Geitzenauer W, et al. Value of polarisation-sensitive optical coherence tomography in diseases affecting the retinal pigment epithelium. *Br J Ophthalmol.* 2008;92:204–209.

37. Srinivasan VJ, Monson BK, Wojtkowski M, et al. Characterization of outer retinal morphology with high-speed, ultrahigh-resolution optical coherence tomography. *Invest Ophthalmol Vis Sci.* 2008; 49:1571–1579.

38. Huang Y, Cideciyan AV, Papastergiou GI, et al. Relation of optical coherence tomography to microanatomy in normal and rd chickens. *Invest Ophthalmol Vis Sci.* 1998;39:2405–2416.

39. Fischer MD, Huber G, Beck SC, et al. Noninvasive, in vivo assessment of mouse retinal structure using optical coherence tomography. *PLoS One.* 2009;4:e7507.

40. Srinivasan VJ, Ko TH, Wojtkowski M, et al. Noninvasive volumetric imaging and morphometry of the rodent retina with high-speed, ultrahigh-resolution optical coherence tomography. *Invest Ophthalmol Vis Sci.* 2006;47:5522–5528.

41. Gloesmann M, Hermann B, Schubert C, Sattmann H, Ahnelt PK, Drexler W. Histologic correlation of pig retina radial stratification with ultrahigh-resolution optical coherence tomography. *Invest Ophthalmol Vis Sci.* 2003;44:1696–1703.

42. Abbott CJ, McBrien NA, Grunert U, Pianta MJ. Relationship of the optical coherence tomography signal to underlying retinal histology in the tree shrew (Tupaia belangeri). *Invest Ophthalmol Vis Sci.* 2009;50:414–423.

43. Chauhan DS, Marshall J. The interpretation of optical coherence tomography images of the retina. *Invest Ophthalmol Vis Sci.* 1999;40:2332–2342.

44. Chen TC, Cense B, Miller JW, et al. Histologic correlation of in vivo optical coherence tomography images of the human retina. *Am J Ophthalmol.* 2006;141:1165–1168.

45. Ghazi NG, Dibernardo C, Ying HS, Mori K, Gehlbach PL. Optical coherence tomography of enucleated human eye specimens with histological correlation: origin of the outer "red line." *Am J Ophthalmol.* 2006;141:719–726.

46. Brown NH, Koreishi AF, McCall M, Izatt JA, Rickman CB, Toth CA. Developing SDOCT to assess donor human eyes prior to tissue sectioning for research. *Graefes Arch Clin Exp Ophthalmol.* 2009;247:1069–1080.

47. Guyton JR, Klemp KF. Ultrastructural discrimination of lipid droplets and vesicles in atherosclerosis: value of osmium-thiocarbohydrazide-osmium and tannic acid-paraphenylenediamine techniques. *J Histochem Cytochem.* 1988;36:1319–1328.

48. Curcio CA, Millican CL, Bailey T, Kruth HS. Accumulation of cholesterol with age in human Bruch's membrane. *Invest Ophthalmol Vis Sci.* 2001;42:265–274.

49. Bagci AM, Shahidi M, Ansari R, Blair M, Blair NP, Zelkha R. Thickness profiles of retinal layers by optical coherence tomography image segmentation. *Am J Ophthalmol.* 2008;146:679–687.

50. Drasdo N, Millican CL, Katholi CR, Curcio CA. The length of Henle fibers in the human retina and a model of ganglion receptive field density in the visual field. *Vision Res.* 2007;47:2901–2911.

51. Bland JM, Altman DG. Statistical methods for assessing agreement between two methods of clinical measurement. *Lancet.* 1986;1:307–310.

52. Wojtkowski M, Srinivasan V, Ko T, Fujimoto J, Kowalczyk A, Duker J. Ultrahigh-resolution, high-speed, Fourier domain optical coherence tomography and methods for dispersion compensation. *Opt Express.* 2004;12:2404–2422.

53. Fleckenstein M, Charbel Issa P, Helb HM, et al. High-resolution spectral domain-OCT imaging in geographic atrophy associated with age-related macular degeneration. *Invest Ophthalmol Vis Sci.* 2008;49:4137–4144.

54. Falkenberry SM, Ip MS, Blodi BA, Gunther JB. Optical coherence tomography findings in central retinal artery occlusion. *Ophthalmic Surg Lasers Imaging.* 2006;37:502–505.

55. Margolis R, Spaide RF. A pilot study of enhanced depth imaging optical coherence tomography of the choroid in normal eyes. *Am J Ophthalmol.* 2009;147:811–815.

56. Curcio CA, Sloan KR, Kalina RE, Hendrickson AE. Human photoreceptor topography. *J Comp Neurol.* 1990;292:497–523.

57. Sarks JP, Sarks SH, Killingsworth MC. Evolution of geographic atrophy of the retinal pigment epithelium. *Eye.* 1988;2:552–577.

58. Curcio CA, Presley JB, Millican CL, Medeiros NE. Basal deposits and drusen in eyes with age-related maculopathy: evidence for solid lipid particles. *Exp Eye Res.* 2005;80:761–775.

59. Curcio CA, Millican CL. Basal linear deposit and large drusen are specific for early age-related maculopathy. *Arch Ophthalmol.* 1999;117:329–339.

60. Sarks SH. Ageing and degeneration in the macular region: a clinicopathological study. *Br J Ophthalmol.* 1976;60:324–341. PMID 952802.

61. van der Schaft TL, Mooy CM, de Bruijn WC, Oron FG, Mulder PGH, de Jong PTVM. Histologic features of the early stages of age-related macular degeneration. *Ophthalmol.* 1992;99:278–286.

62. Spraul CW, Grossniklaus HE. Characteristics of drusen and Bruch's membrane in postmortem eyes with age-related macular degeneration. *Arch Ophthalmol.* 1997;115:267–273.

63. Malek G, Li C-M, Guidry C, Medeiros NE, Curcio CA. Apolipoprotein B in cholesterol-containing drusen and basal deposits in eyes with age-related maculopathy. *Am J Pathol.* 2003;162:413–425.

64. Huang Y, Cideciyan AV, Aleman TS, et al. Optical coherence tomography (OCT) abnormalities in rhodopsin mutant transgenic swine with retinal degeneration. *Exp Eye Res.* 2000;70:247–251.

65. Giani A, Cigada M, Choudhry N, et al. Reproducibility of retinal thickness measurements on normal and pathologic eyes by different optical coherence tomography instruments. *Am J Ophthalmol.* 2010;150:815–824.

66. Grover S, Murthy RK, Brar VS, Chalam KV. Comparison of retinal thickness in normal eyes using Stratus and Spectralis optical coherence tomography. *Invest Ophthalmol Vis Sci.* 2010;51:2644–2647.

67. Hendrickson A. Organization of the human fovea. In: Penfold PL, Provis JM, eds. *Macular Degeneration.* Berlin: Springer-Verlag; 2005:1–24.

68. Curcio CA, Allen KA. Topography of ganglion cells in human retina. *J Comp Neurol.* 1990;300:5–25.

69. Wässle H, Grünert U, Rohrenbeck J, Boycott BB. Cortical magnification factor and the retinal ganglion cell density in the primate. *Nature.* 1989;341:643–646.

70. Hsu A, Tsukamoto Y, Smith RG, Sterling P. Functional architecture of primate cone and rod axons. *Vision Res.* 1998;38:2539–2549.

71. Wassle H. Parallel processing in the mammalian retina. *Nat Rev Neurosci.* 2004;5:747–757.

72. Pircher M, Gotzinger E, Leitgeb R, Sattmann H, Findl O, Hitzenberger C. Imaging of polarization properties of human retina in vivo with phase resolved transversal PS-OCT. *Opt Express.* 2004;12:5940–5951.

73. Pircher M, Gotzinger E, Findl O, et al. Human macula investigated in vivo with polarization-sensitive optical coherence tomography. *Invest Ophthalmol Vis Sci.* 2006;47:5487–5494.

74. Lujan B, Roorda A, Knighton RW, Carroll J. Revealing Henle's fiber layer using spectral domain optical coherence tomography. *Invest Ophthalmol Vis Sci.* 2011;52:1486–1492.

75. Otani T, Yamaguchi Y, Kishi S. Improved visualization of Henle fiber layer by changing the measurement beam angle on optical coherence tomography. *Retina.* 2010.

76. Spaide RF. Age-related choroidal atrophy. *Am J Ophthalmol.* 2009;147:801–810.

77. Ramrattan RS, van der Schaft TL, Mooy CM, de Bruijn WC, Mulder PGH, de Jong PTVM. Morphometric analysis of Bruch's membrane, the choriocapillaris, and the choroid in aging. *Invest Ophthalmol Vis Sci.* 1994;35:2857–2864.

78. Thumann G, Hoffman S, Hinton DR. Cell biology of the retinal pigment epithelium. In: Ryan SJ, ed. *Retina.* St. Louis: Mosby; 2006:1041–1074.

79. Feeney-Burns L, Burns RP, Gao C-L. Age-related macular changes in humans over 90 years old. *Am J Ophthalmol.* 1990;109:265–278.

80. Gao H, Hollyfield JG. Aging of the human retina. Differential loss of neurons and retinal pigment epithelial cells. *Invest Ophthalmol Vis Sci.* 1992;33:1–17.

81. Del Priore LV, Kuo Y-H, Tezel TH. Age-related changes in human RPE cell density and apoptosis proportion in situ. *Invest Ophthalmol Vis Sci.* 2002;43:3312–3318.

82. Harman AM, Fleming PA, Hoskins RV, Moore SR. Development and aging of cell topography in the human retinal pigment epithelium. *Invest Ophthalmol Vis Sci.* 1997;38:2016–2026.

83. Panda-Jonas S, Jonas JB, Jakobczyk-Zmija M. Retinal pigment epithelial cell count, distribution, and correlations in normal human eyes. *Am J Ophthalmol.* 1996;121:181–189.

84. Morgan JI, Dubra A, Wolfe R, Merigan WH, Williams DR. In vivo autofluorescence imaging of the human and macaque retinal pigment epithelial cell mosaic. *Invest Ophthalmol Vis Sci.* 2009;50:1350–1359.

85. Grunwald JE, Hariprasad SM, DuPont J. Effect of aging on foveolar choroidal circulation. *Arch Ophthalmol.* 1998;116:150–154.

86. Fitzgerald ME, Tolley E, Frase S, et al. Functional and morphological assessment of age-related changes in the choroid and outer retina in pigeons. *Vis Neurosci.* 2001;18:299–317.

87. Curcio CA, Millican CL, Allen KA, Kalina RE. Aging of the human photoreceptor mosaic: evidence for selective vulnerability of rods in central retina. *Invest Ophthalmol Vis Sci.* 1993;34:3278–3296.

88. Bringmann A, Pannicke T, Grosche J, et al. Muller cells in the healthy and diseased retina. *Prog Retin Eye Res.* 2006;25:397–424.

89. DiLoreto DA Jr, Martzen MR, del Cerro C, Coleman PD, del Cerro M. Muller cell changes precede photoreceptor cell degeneration in the age-related retinal degeneration of the Fischer 344 rat. *Brain Res.* 1995;698:1–14.

90. Madigan MC, Penfold PL, Provis JM, Balind TK, Billson FA. Intermediate filament expression in human retinal macroglia: histo-

pathologic changes associated with age-related macular degeneration. *Retina.* 1994;14:65–74.

91. Wu KH, Madigan MC, Billson FA, Penfold PL. Differential expression of GFAP in early v late AMD: a quantitative analysis. *Br J Ophthalmol.* 2003;87:1159–1166.

92. Grosche J, Grimm D, Clemens N, Reichenbach A. Retinal light damage vs. normal aging of rats: altered morphology, intermediate filament expression, and nuclear organization of Muller (glial) cells. *J Hirnforsch.* 1997;38:459–470.

93. Harwerth RS, Wheat JL. Modeling the effects of aging on retinal ganglion cell density and nerve fiber layer thickness. *Graefes Arch Clin Exp Ophthalmol.* 2008;246:305–314.

94. Harwerth RS, Wheat JL, Rangaswamy NV. Age-related losses of retinal ganglion cells and axons. *Invest Ophthalmol Vis Sci.* 2008; 49:4437–4443.

95. Guidry C, Medeiros NE, Curcio CA. Phenotypic variation of retinal pigment epithelium in age-related macular degeneration. *Invest Ophthalmol Vis Sci.* 2002;43:267–273.

96. Fujiwara T, Imamura Y, Margolis R, Slakter JS, Spaide RF. Enhanced depth imaging optical coherence tomography of the choroid in highly myopic eyes. *Am J Ophthalmol.* 2009;148: 445–450.

97. Budenz DL, Anderson DR, Varma R, et al. Determinants of normal retinal nerve fiber layer thickness measured by Stratus OCT. *Ophthalmology.* 2007;114:1046–1052.

98. Alamouti B, Funk J. Retinal thickness decreases with age: an OCT study. *Br J Ophthalmol.* 2003;87:899–901.

99. Neuville JM, Bronson-Castain K, Bearse MA Jr, et al. OCT reveals regional differences in macular thickness with age. *Optom Vis Sci.* 2009;86:E810–E816.